Synthesis, crystal structure, and electrode characteristics of LiMnPO$_4$(OH) cathode for lithium batteries

Yang Yang [a], Masaaki Hirayama [a], Masao Yonemura [b], Ryoji Kanno [a,*]

[a] Department of Electronic Chemistry, Interdisciplinary Graduate School of Science and Engineering, Tokyo Institute of Technology, 4259 Nagatsuta, Midori-ku, Yokohama 226-8502, Japan.
[b] KEK, Tokai, Ibaraki 319-1195, Japan.

ARTICLE INFO

ABSTRACT

The electrochemical properties of lithium manganese hydroxyphosphate, LiMnPO$_4$(OH), with the tavorite structure have been investigated to assess its suitability as a cathode material for lithium batteries. Stoichiometric LiMnPO$_4$(OH) was synthesized by an ion-exchange reaction with MnPO$_4 \cdot$ H$_2$O and LiNO$_3$. Lithium (de)intercalation reaction was observed for the first time in the trivalent LiMnPO$_4$(OH), and it exhibited a reversible capacity of 110 mA h g^{-1} with an average cell voltage of 3.4 V (vs. Li) after an irreversible phase change during the first charge process. The crystal structure has been refined at room temperature by neutron and synchrotron X-ray diffraction data using Rietveld method with a space group of $P-1$. The hydroxy group at a bottleneck may reduce the attraction force between lithium and the bottleneck oxygen ions that thus increase the ion mobility along the lithium diffusion tunnel.

1. Introduction

Research on intercalation materials for lithium batteries has progressed considerably since their successful application in various mobile electronic devices. Various lithium transition-metal oxides, LiMO$_2$ (M=Co, Ni, Mn) [1–3] with a layered rock-salt structure, LiMn$_2$O$_4$ [4] with a spinel structure, and their substituted derivatives have been extensively investigated as positive electrode materials. On the other hand, following the development of an olivine LiFePO$_4$ cathode [5], a wide variety of polyanionic materials have been investigated as promising new cathode materials. In particular, PO$_4^{3-}$-based compounds have been studied because they enhance the redox potential and hence the energy density due to the strong inductive effect of the phosphate group [6]. In addition, their three-dimensional framework consists of corner-sharing octahedra and tetrahedra, which imparts a high structural stability during lithium insertion/extraction [5,7].

Of phosphate-based materials, LiMPO$_4$(OH) (M=Mn, Fe) with the tavorite structure are particularly promising cathode materials for lithium batteries as they have a theoretical capacity of ca. 160 mA h g^{-1} and a structure characteristic for high lithium ion mobility. The three-dimensional framework consists of MO$_6$ octahedral chains bridged by PO$_4$ tetrahedra, which provides two possible lithium sites in diffusion tunnels. The hydroxy group OH$^-$ in LiMPO$_4$(OH) along the bottleneck might enhance lithium ion hopping due to the small interaction between Li and the framework due to the lower charge of OH$^-$ groups relative to O^{2-} ions. Tavorite compounds with OH$^-$ groups might be another strategy for obtaining high-performance (in particular, a high-rate) electrodes for lithium batteries.

LiFePO$_4$(OH) with the tavorite structure has recently been reported to have a discharge capacity of ca. 100 mA h g^{-1} (0.7 mol Li$^+$) at a voltage of ~2.3 V (vs. Li$^+$/Li) [8]. However, the amount of lithium extracted from the compound was limited because of the difficulty in oxidizing Fe(III) to Fe(IV). On the other hand, the manganese isomorph, LiMnPO$_4$(OH) [9], may have a higher capacity since Mn^{3+} ions can be oxidized to Mn^{4+} under conventional charge–discharge conditions with a higher redox potential [10]. Crystal structure of LiMnPO$_4$(OH) has been studied by Aranda et al., using neutron diffraction and a deuterium (D) substitution of protium (H) [11]. The lithium ions have been located in the channel along [1 0 1] direction and D/H have been bonded to oxygen atoms with covalent and hydrogen bonding within the structure with a space group of $C-1$. LiMnPO$_4$(OH) has exhibited high ionic conductivity as high as 3×10^{-5} S cm^{-1} [12], which can be compared with that of transition metal oxides, such as LiMn$_2$O$_4$ [13]. Although the diffusion mechanism remains unknown, the conductivity is considered to be related to its wide diffusion channel in the crystal structure. Furthermore, no systematic studies on its electrode behavior or (de)intercalation characteristics have been reported.

* Corresponding author. Fax: +81 45 924 5401.
E-mail addresses: yang@echem.titech.ac.jp (Y. Yang),
hirayama@echem.titech.ac.jp (M. Hirayama), yone@post.kek.jp (M. Yonemura),
kanno@echem.titech.ac.jp (R. Kanno).

In the present study, LiMnPO$_4$(OH) nanoparticles were synthesized and their electrochemical de(intercalation) properties were investigated. Their structures were characterized by neutron and synchrotron X-ray diffraction (XRD) analyses. Preliminary reaction mechanism during initial charge/discharge is discussed based on the charge–discharge and *ex-situ* XRD data.

2. Experimental

LiMnPO$_4$(OH) was synthesized by the H$^+$/Li$^+$ exchange reaction of MnPO$_4 \cdot$H$_2$O and LiNO$_3$ [9]. MnPO$_4 \cdot$H$_2$O was prepared by a hydrothermal method [14] using Mn(NO$_3$)$_2$ (Wako, Ltd.; > 98 wt.%) and H$_3$PO$_4$ (Wako, Ltd.; > 85 wt.%) at 160 °C. The obtained MnPO$_4 \cdot$H$_2$O was then mixed with LiNO$_3$ (Wako, Ltd.; > 98 wt.%) in the molar ratio of 1:4 by ball milling for 2 h. The precursor was heated at 200 °C in air, washed with distilled water, and dried in vacuum at 60 °C. The brownish LiMnPO$_4$(OH) phase was obtained.

XRD patterns were collected at room temperature using a Rigaku SmartLab powder diffractometer with Cu $K\alpha$ radiation in the 2θ range of 10 to 70° with a step scan with an interval of 0.02° for a counting time of 3 s. The phase transition during the electrode reaction was investigated by XRD measurements at different charge/discharge states between 4.6 and 2.0 V. To avoid exposing them to oxygen or water, the electrodes films were placed in a Kapton folder filled with argon gas. The electrode films were obtained from coin cells; the cells were disassembled in an Ar-filled glove box after they had been charged or discharged to a fixed potential. The films were rinsed several times in anhydrous dimethyl carbonate to eliminate residual salts, dried at room temperature, and used in XRD measurements.

Inductively coupled plasma (ICP) atomic emission spectrometry analysis was used for elemental analysis of Li, Mn, and P using a Prodigy ICP atomic emission spectrometer. Spectra were obtained after the LiMnPO$_4$(OH) powder had been completely dissolved in a hydrochloric acid solution. The amount of hydroxy group in the ion-exchanged phase was confirmed by thermogravimetry–differential thermal analysis (TG-DTA) with a Rigaku Instrument Thermo plus TG 8120 at a heating rate of 5 °C min^{-1} in an argon atmosphere. The morphologies of powder samples were investigated by high-resolution scanning electron microscopy (SEM) observations using a Hitachi S-4700 microscope. Carbon coating treatment was carried out to decrease charging up of the samples during SEM observations.

The crystal structure was investigated by synchrotron-radiation (SR) XRD measurements at the High-Energy Accelerator Research Center (KEK) in Tsukuba (Japan) on the high-resolution powder diffractometer installed in beam line BL-4B$_2$ with a multiple-detector system [15,16]. Diffraction data was collected at room temperature with a wavelength of 1.1971 Å in the angular range of 0–100° with a 0.01° (2θ) step and an accumulation time of 6 h. Time-of-flight neutron diffraction (TOF-ND) measurements were performed to determine the position of the hydrogen ions using the neutron diffractometer (iMATERIA) at J-Parc (Tokai, Japan). The sample was inserted in an 8-mm-diameter vanadium tube and measurements were performed in transmission mode at room temperature. The SR-XRD and neutron diffraction data were analyzed by Rietveld refinement using the structural model Li$_{2i}$[(Mn1)$_{1a}$(Mn2)$_{1b}$](P)$_{2i}$(O)$_{2i}$(H)$_{2i}$ (space group: $P-1$) [17] and the programs Rietan-FP [18] and Z-Rietveld [19], respectively. The split pseudo-Voigt function proposed by Toraya [20] and the pseudo-Voigt function proposed by Thompson et al., [21] were used in the refinements of the SR-XRD and neutron diffraction data, respectively.

The electrochemical performances were investigated by performing charge–discharge measurements using 2032 coin cells assembled in an argon-filled glove box. The cells were aged for 24 h at room temperature before performing charge–discharge tests. The negative electrode was a disk of lithium metal foil. A polypropylene separator (Celgard) soaked in a solution of 1 mol l^{-1} LiPF$_6$ in ethylene carbonate/diethyl carbonate (3:7vol.%) was placed between the two electrodes. A positive electrode was fabricated by mixing 80 wt% of the active material LiMnPO$_4$(OH) and 15 wt% of Ketjen Black (ECP, Akzo Nobel) with 5 wt% polyvinylidene fluoride in N-methylpyrrolidone. Strong mixing between the active material and the carbon powder was achieved by ball milling the mixture for 60 min at 240 rpm using a Fritsch ball mill. The obtained slurry was spread onto a 20 μm thick aluminum foil using a doctor blade with a blade height of 50 μm. The electrode was obtained after drying at 120 °C in a vacuum for 6 h. The electrode was cut into a ø15.95 mm disk and then cold pressed at 300 kg cm^{-2} in a uniaxial press. All electrodes contained about 1.2 mg of active material with a thickness of about 3 μm. The charge–discharge characteristics were examined at room temperature over a voltage range of 2.0 to 4.6 V vs. Li$^+$/Li at a constant rate of 1/100 C (corresponding to a theoretical exchange of one electron per formula during charging or discharging for 100 h). To evaluate the rate characteristics of the LiMnPO$_4$(OH) electrode, cells were charged and discharged at various current rates between 1/100 and 10 C.

3. Results and discussion

Fig. 1 shows XRD patterns of the hydrate precursor and the product of the ion-exchange reaction. All diffraction peaks of the ion-exchange reaction product were indexed with the space group $P-1$, which is consistent with the XRD pattern of LiMn-PO$_4$(OH) reported previously [14]. The structure changed from being monoclinic ($C2/c$) for MnPO$_4 \cdot$o$_2$O to being triclinic ($P-1$) for LiMnPO$_4$(OH) with the H$^+$/Li$^+$ exchange reaction. The diffraction peaks broadened slightly on ion exchange; the full widths at half maximum of the -111, 110, and 010 diffraction peaks increased from 0.05, 0.08, and 0.09° for MnPO$_4 \cdot$H$_2$O to 0.12, 0.14, and 0.15° for LiMnPO$_4$(OH), respectively. This indicates that the crystal lattice strain increased or the particle size decreased during the H$^+$/Li$^+$ exchange reaction. Fig. 2(a) and (b) show SEM images of LiMnPO$_4$(OH) and MnPO$_4 \cdot$H$_2$O, respectively. MnPO$_4 \cdot$H$_2$O exhibits a rod-like morphology with a particle size
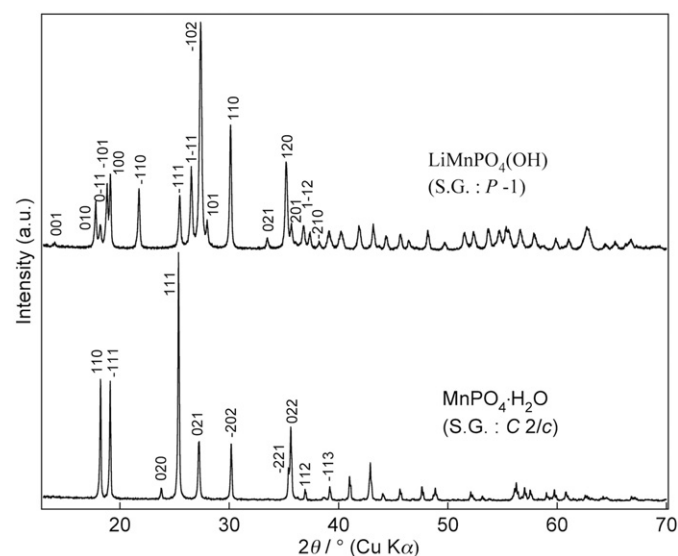
Fig. 1. XRD patterns of MnPO$_4 \cdot$H$_2$O and LiMnPO$_4$(OH).
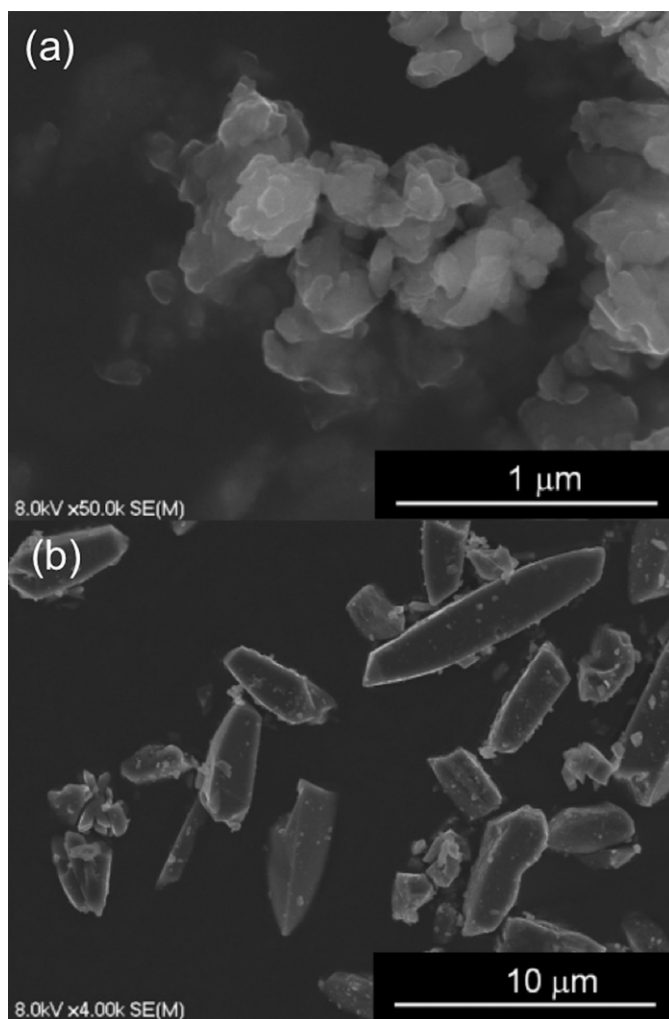
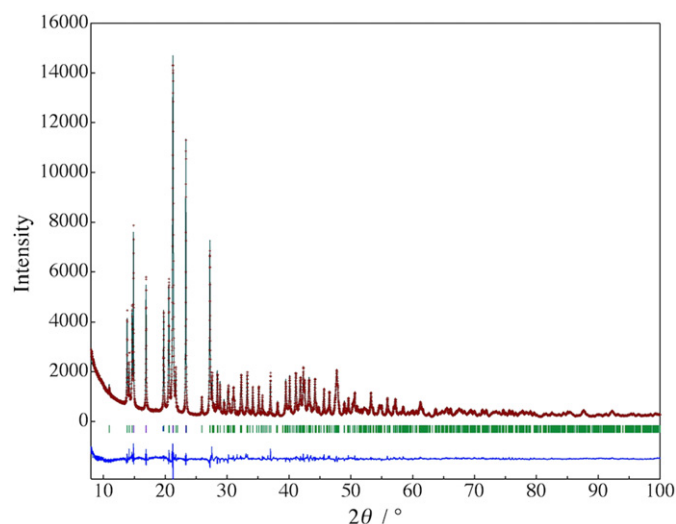**Fig. 2.** SEM images of (a) LiMnPO$_4$(OH) and (b) MnPO$_4\cdot$H$_2$O.

Fig. 3. Observed (plus symbols), calculated (solid line), and difference (bottom) profiles for the Rietveld refinement from synchrotron X-ray diffraction data of the LiMnPO$_4$(OH). The short vertical lines below the profiles indicate the peak positions of all possible Bragg reflections.
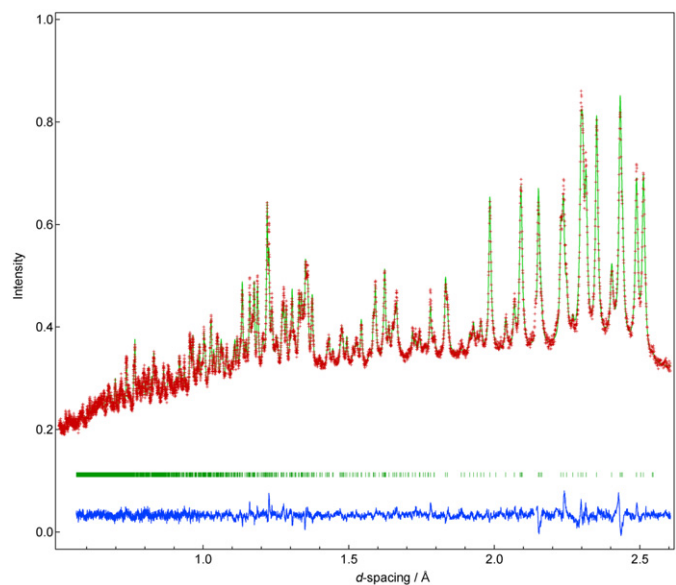

Fig. 4. Observed (plus symbols), calculated (solid line), and difference (bottom) profiles for the Rietveld refinement from time-of-flight neutron diffraction data for LiMnPO$_4$(OH). The short vertical lines below the profiles indicate the peak positions of all possible Bragg reflections.

of few micrometers, whereas LiMnPO$_4$(OH) has an irregular and agglomerated morphology with particle sizes of less than a few hundreds of nanometers. ICP measurements clarified that Li/Mn/P are present in molar ratios of 0.98(2)/0.98(1)/1. The amount of hydroxy group in the ion-exchanged phase was confirmed by TG analysis. The weight loss in the TG curve was -10.1% (see the Supporting Information S1), which is in good agreement with that of -9.8% caused by one OH group decomposition in LiMn-PO$_4$(OH) [9]. These results suggest that the nanoparticles of LiMnPO$_4$(OH) have a composition close to the stoichiometry by ion-exchange reaction.

The SR-XRD data were refined based on a previously reported structure [17] with cation mixing between Mn and Li ions. A structural model with the space group $P-1$ was used for refinement as follows: Li in 2i (0.24, 0.618, 0.23); Mn1 in 1a (0, 0, 0); Mn2 in 1b (0, 0, 0.5); P in 2i (-0.324, 0.371, 0.235); O$_1$ in 2i (0.1106, 0.6462, -0.121); O$_2$ in 2i (-0.6945, -0.2375, 0.6004); O$_3$ in 2i (0.3028, 0.3406, -0.337); O$_4$ in 2i (-0.3671, -0.2479, 0.9442); O$_5$ in 2i (0.1656, -0.0306, 0.2813); H in 2i (0.3744, 0.0738, 0.3454). The positions of the hydrogen atoms were fixed at their initial positions during X-ray Rietveld refinement. Fig. 3 shows the synchrotron Rietveld refinement results for LiMnPO$_4$(OH). The profile fittings provide a good agreement factor, R_{wp} of 6.21% ($R_{Bragg}=4.54\%$) with a goodness of fit value $S=R_{wp}/R_e=1.37$. The refined lattice parameters are $a=5.1249(7)$ Å, $b=5.4512(9)$ Å, $c=7.1085(2)$ Å, $\alpha=106.244(14)$, $\beta=108.169(12)°$, $\gamma=101.297(13)°$. ($V=172.21(5)$ Å^3). Li and Mn

ions, respectively, occupy the 2i and 1a/1b sites, indicating that no cation mixing occurs between the Li and Mn sites. Based on the structure obtained from analysis of the SR-XRD data, the positions and contents of protons and lithium ions were determined by neutron Rietveld refinement. Fig. 4 shows the neutron Rietveld refined pattern for LiMnPO$_4$(OH). Refinement of 55 profile and structural parameters converged to a weighted profile factor R_{wp} of 2.23% ($R_p=1.79\%$) with a goodness of fit value $S=1.78$ ($S=R_{wp}/R_e$). The structure parameters determined from the final neutron diffraction results are summarized in a CIF format (see the Supporting Information S2).

Protons are determined to be at the 2i site (0.3762(4), 0.0844(5), 0.3509(4)) of stoichiometric LiMnPO$_4$(OH). Protons have an isotropic temperature factor, U_{iso}, of 0.557, which is smaller than that (3.3) of lithium at the 2i site. The total valences

of the atoms at different sites are calculated based on the bond-length-strength theory [22]. Table 1 lists the sum of the bond valences at each site. The value of −1.3 at O(5) is lower than those of other oxygen sites, indicating that the O(5) sites are closely related to the proton sites. These results are consistent with the O(5)–H bond length of 1.085(2) Å obtained by the structural analysis.

Fig. 5 represents a schematic diagram of the LiMnPO₄(OH) crystal structure, which was created with the structure parameters determined from the final neutron diffraction results. The protons are connected to the oxygen O(5), which is shared by two adjacent MnO₆ octahedrons with a H–O(5) distance of 1.085(2) Å. The distance of 1.682(10) Å between O(2) and protons indicates the presence of hydrogen bonding. The proton environment is thus represented by O(5)–H···O(2) with a O–H···O angle of 163.6°. The Li ion, located in the 2i site, is surrounded by six oxygen atoms, forming a distorted octahedron. This site is calculated to have a valence sum of 0.96(1), which is consistent with ionic bonding in the LiO₆ octahedra. Fig. 5(b) and (c) shows the unit structure of LiMnPO₄(OH) and (a) one-dimensional tunnel along the [1 0 0] direction. The LiMnPO₄(OH) has a zigzag lithium diffusion pathway along the [1 0 0] direction through the LiO₆ octahedra (2i sites) and a vacant octahedral site formed by O(1), O(3), and O(4) sites, where the LiO₆ octahedron shares an edge with the vacant octahedron and the MnO₆ octahedron.

Lithium ions could migrate along the zigzag path through the vacant sites (dashed line) and through a bottleneck formed by the O(1), O(4), and O(5) sites (red triangles). The H atoms exist near the O(5) site and form hydroxide ions O–H⁻ in the bottleneck of lithium diffusion pathway. This probably reduces the attractive Coulomb force between O–H⁻ and Li⁺ ions that might facilitate Li migration.

Fig. 6 shows the charge–discharge characteristics of a LiMnPO₄(OH) electrode measured at 25 °C between 2.0 and 4.6 V (vs. Li⁺/Li) at a rate of 1/100 C. The charge–discharge curves exhibit different profiles and there is a large difference between the capacities of the initial and subsequent cycles. In the initial charge, the voltage increases rapidly to about 3.8 V and then increases gradually to the cut-off voltage of 4.6 V. Only half its theoretical capacity 80 mAh g⁻¹ (ca. 0.6 lithium per LiMnPO₄(OH)

Table 1
Bond valence sums in LiMnPO₄(OH).

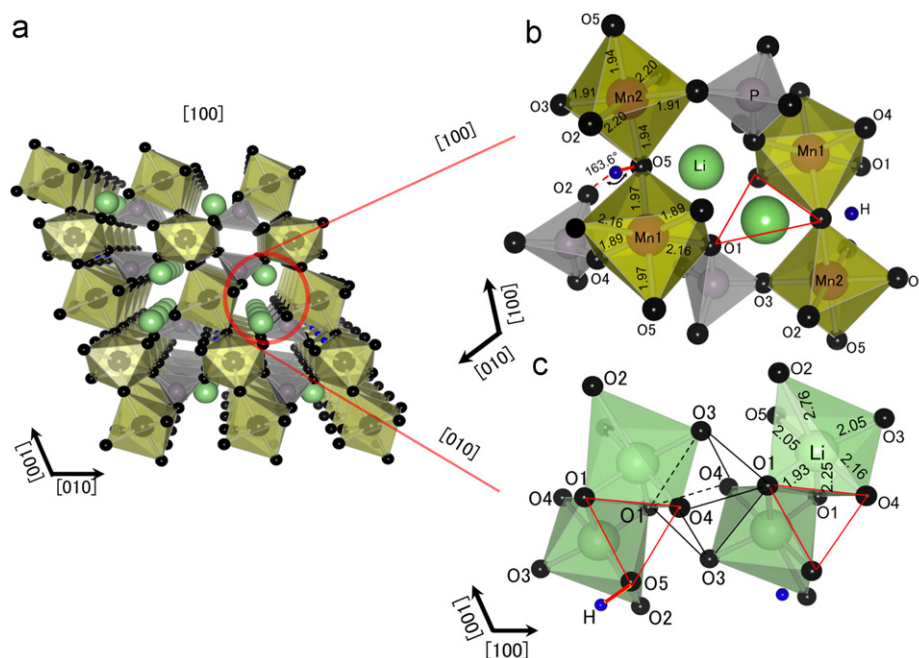|	
Li in 2i site	1.0
Mn1 in 1a site	3.0
Mn2 in 1b site	3.0
P1 in 2i site	5.0
O₁ in 2i site	−1.9
O₂ in 2i site	−1.9
O₃ in 2i site	−2.0
O₄ in 2i site	−2.0
O₅ in 2i site	−1.3

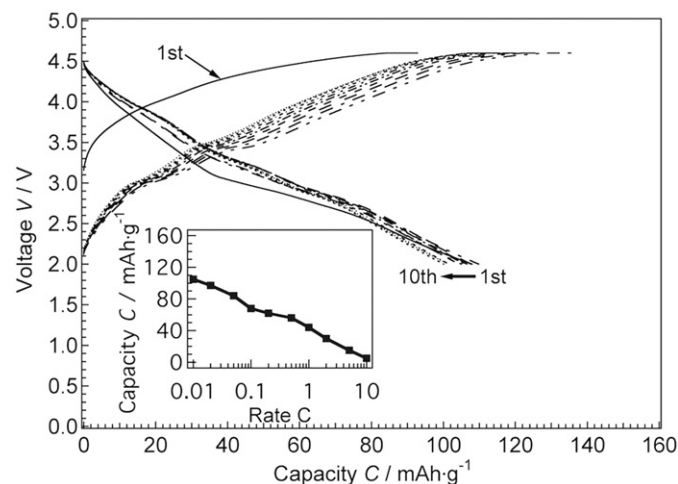**Fig. 6.** Charge–discharge curves for the Li/LiMnPO₄(OH) cell up to 10 cycles measured at 25 °C under a C/100 rate. The inset shows the rate capability of the LiMnPO₄(OH) cathode.

Fig. 5. Crystal structure of LiMnPO₄(OH); (a) perpendicular view of the framework along the [1 0 0] direction, (b) the detail of manganese environment, and (c) lithium environment in possible diffusion pathway along [1 0 0] direction (bond lengths are given in Å).

unit) was obtained. In contrast, a sloppy voltage profile was obtained during discharging. With further lithium insertion into the host structure when the $LiMnPO_4(OH)$/Li cell was discharged to 2.0 V, the discharge profile shows another voltage plateau at about 3 V. Furthermore, an initial discharge capacity of 110 mA h g^{-1} was observed, which is larger than the first charge capacity of 80 mA h g^{-1}. After the initial charge–discharge cycle, the electrode reaction shows reversible behavior with a steady capacity retention on cycling.

The rate capability was investigated for Li/Li$^+$/$LiMnPO_4(OH)$ cells with different discharge current densities. The inset of Fig. 6 shows discharge curves as a function of the C rate. Although the capacity at a rate of 1 C decreases to about 50% of the initial capacity, no significant capacity retention was observed for the capacity obtained at a rate of 1/100 C after being tested under a current density at a rate of 10 C. This suggests that the capacity deterioration at high current rates may be attributed to its poor electron conductivity (9.6×10^{-7} S cm^{-1}, as measured at room temperature by the dc four-probe method). It may be possible to realize high electrode performance by further optimizing the cell, such as applying carbon coating to improve its electrical conductivity [23].

Fig. 7 shows a differential plot (dQ/dV) of the first, second, and fifth cycles of the charge–discharge curves for the Li/Li$^+$/$LiMnPO_4(OH)$ cell. In the initial cycle, a pair of weak redox peaks, A1b and C1b, is observed at a voltage near 4.0 V. A weak cathodic peak, C1a, appears at about 4.3 V. When the cell is discharged to 2.0 V, two reduction peaks C1c and C1d were observed at 2.6 and 2.9 V, respectively. Two pairs of strong redox peaks, A2c and C2c at a voltage of about 3.3 V and A2d and C2d at about 2.9 V, developed during the second cycle, which indicates that there are several reaction steps between 2.0 and 4.0 V. The intensities of the redox peaks gradually decrease with cycling, which agrees well with the capacity deterioration in the second cycle. The higher discharge capacity than that of the first charging process may correspond to the increase in the reversible redox pairs around 2.9 and 3.3 V, indicating a two-step phase change during charging and discharging. The irreversible phase change in the

first charge process causes a phase with higher capacity where the intercalation proceeds reversibly by two-step phase changes. The first reduction process might introduce a redox couple of Mn^{2+}/Mn^{3+} together with Mn^{3+}/Mn^{4+}, which also increases the total capacity of the material. The higher charge–discharge capacity of manganese tavorite than the iron system might be due to the stability of the tetravalent ions in the manganese system; these ions produce the first charge capacity that provides a reversible reaction during the charge–discharge cycle.

XRD measurements were used to examine the phase changes in $LiMnPO_4(OH)$ during the initial charge/discharge. Fig. 8(b) and (c) shows XRD patterns of $LiMnPO_4(OH)$ after being charged to 4.6 V and discharged to 2.0 V in the first cycle, respectively. All the reflections can be indexed by the space group $P-1$, indicating that the phase transformed after the charge–discharge reaction has the structure with the same space group as that of $LiMnPO_4(OH)$. The XRD peaks of the charged sample are shifted to slightly to higher 2θ values. The lattice parameters changed from $a=5.126$, $b=5.453$, and $c=7.109$ Å for the pristine sample to $a=5.116$, $b=5.439$, and $c=7.099$ Å for the charged sample, indicating lithium extraction from the host structure accompanied by a partial oxidation from Mn^{3+} to Mn^{4+}. The XRD peaks of the discharged sample shift to lower 2θ values and to lattice constants of $a=5.138$, $b=5.476$, and $c=7.115$ Å. These results suggest that the phase after transformation permits the extration/intercalation of lithium ions with shrinking/expanding of crystal lattice during charge/discharge. On the other hand, the intensity ratio of 100 and 010 reflection decreased from 1.68 to 1.16 and the value of $100/-101$ from 1.64 to 0.88 after the pristine was discharged to 2.0 V, whereas their width increase. The variation in intensity and width of reflections indicate a structure change of $LiMnPO_4(OH)$ during charge–discharge, although the phase transformed after the initial charge–discharge reaction still has the same space group with that of $LiMnPO_4(OH)$. The details in the phase transition during charge–discharge reaction need further study by in-situ SR-XRD and precise crystal structure refinement, which could supply more informative data than the low resolution diffraction data obtained from XRD measurement in laboratory.
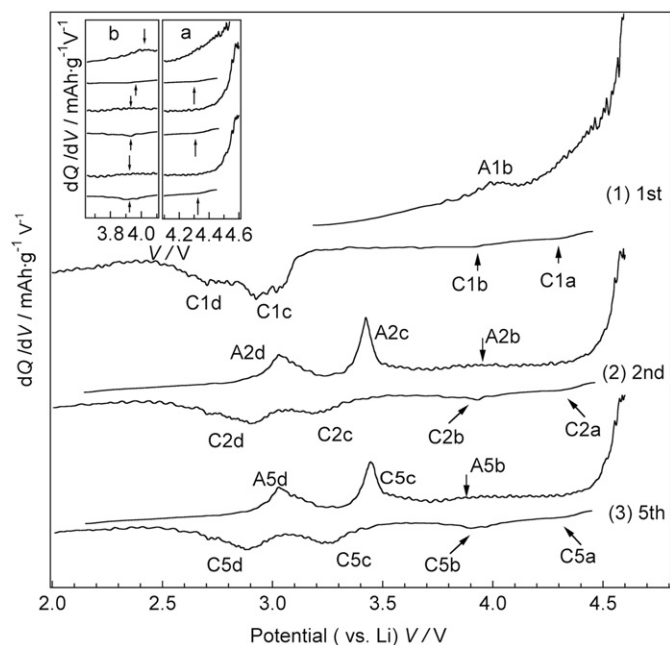

Fig. 7. Differential capacity curves on cycling for $LiMnPO_4(OH)$ tested between 2.0 and 4.6 V (vs. Li$^+$/Li) at a rate of C/100 for (1) initial, (2) second, and (3) fifth cycles.

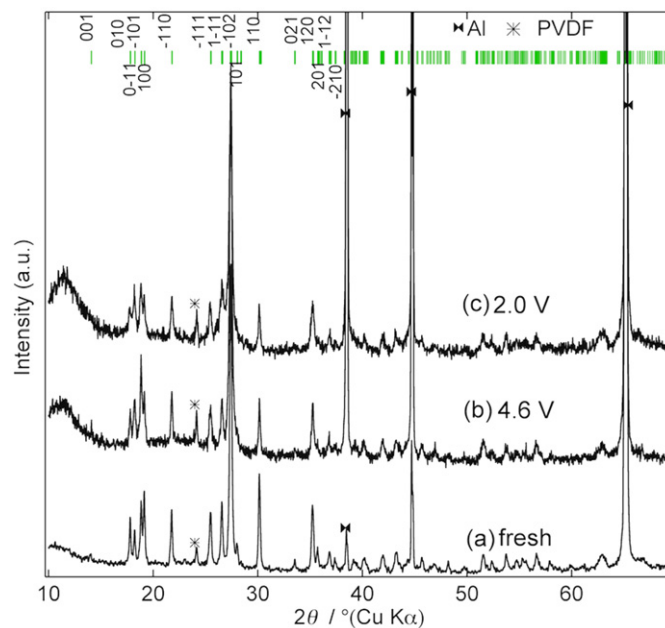Fig. 8. XRD patterns of $LiMnPO_4(OH)$: (a) pristine, (b) after being charged to 4.6 V in the first cycle, and (c) after being discharged to 2.0 V in the first cycle.

4. Conclusions

Nano-sized $LiMnPO_4(OH)$ has been synthesized by Li^+/H^+ ion exchange of the hydrate precursor $MnPO_4 \cdot H_2O$. The neutron and synchrotron X-ray diffraction measurements revealed that the hydroxy group situates at a bottleneck and may reduce the attraction force between lithium and the bottleneck oxygen ions, which increases the ion mobility along the diffusion tunnel. The electrochemical properties of $LiMnPO_4(OH)$ were investigated. A capacity of 110 mA h g^{-1} with an average voltage of 3.4 V vs. Li was obtained without carbon coating, indicating lithium (de)intercalation in the trivalent system, $LiMnPO_4(OH)$. The electrochemical and the XRD results suggest an irreversible phase transition during the first charge process from 2.0 to 4.6 V, followed by a reversible electrochemical intercalation after the first discharge cycle.

Acknowledgments

Appendix A. Supplementary materials

Supplementary materials associated with this article can be found in the online version at doi:10.1016/j.jssc.2011.12.023.

References

[1] K. Mizushima, P.C. Jones, P.J. Wiseman, J.B. Goodenough, Mater. Res. Bull. 15 (1980) 783–789.
[2] J.R. Dahn, U. von Sacken, M.W. Juzkow, H. Al-Janaby, J. Electrochem. Soc. 138 (1991) 2207–2211.
[3] A.R. Armstrong, P.G. Bruce, Nature 381 (1996) 499–500.
[4] M.M. Thackeray, W.I.F. David, P.G. Bruce, J.B. Goodenough, Mater. Res. Bull. 18 (1983) 461–472.
[5] A.K. Padhi, K.S. Nanjundaswamy, J.B. Goodenough, J. Electrochem. Soc. 144 (1997) 1188–1194.
[6] A.K. Padhi, K.S. Nanjundaswamy, C. Masquelier, S. Okada, J.B. Goodenough, J. Electrochem. Soc. 144 (1997) 1609–1613.
[7] A. Yamada, S.C. Chung, K. Hinokuma, J. Electrochem. Soc. 148 (2001) A224–A229.
[8] N. Marx, L. Croguennec, D. Carlier, E. Suard, A. Wattiaux, F. Le Cras, C. Delmas, Dalton Trans. 39 (2010) 5108–5116.
[9] M.A.G. Aranda, J.P. Attfield, S. Bruque, Angew.Chem. Int. Ed. Engl. 31 (1992) 1090–1092.
[10] B. Ammundsen, J. Paulsen, Adv. Mater. 13 (2001) 943–956.
[11] M.A.G. Aranda, S. Bruque, J.P. Attfield, F. Palacio, R.B.V. Dreele, J. Solid State Chem. 132 (1997) 202–212.
[12] M.A.G. Aranda, S. Bruque, J.P. Attfield, J.R. Ramos-Barrado, Solid State Ionics 407 (1993) 63–65.
[13] M.Y. Saidi, J. Barker, R. Koksbang, J. Solid State Chem. 122 (1996) 195–199.
[14] Y.G. Zhang, L. Yi, S.Q. Fu, F. Guo, Bull. Chem. Soc. Jpn. 79 (2006) 270–275.
[15] T. Ida, J. Appl. Crystallogr. 38 (2005) 795–803.
[16] H. Toraya, H. Hibino, K. Ohsumi, J. Synchrotron Radiat. 3 (1996) 75–83.
[17] M.A.G. Aranda, J.P. Attfield, S. Bruque, Powder Diffr. 8 (1993) 155–159.
[18] F. Izumi, T. Ikeda, Mater. Sci. Forum 198 (2000) 321–324.
[19] R. Oishi, M. Yonemura, Y. Nishimaki, S. Torii, A. Hoshikawa, T. Ishigaki, T. Morishima, K. Mori, T. Kamiyama, Nuclear Instrum. Methods Phys. Res. A, Detectors and associated equipment 600 (2009) 189–191.
[20] H. Toraya, J. Appl. Crystallogr. 23 (1990) 485–491.
[21] P. Thompson, D.E. Cox, J.B. Hastings, J. Appl. Crystallogr. 20 (1987) 79–83.
[22] I.D. Brown, R.D. Shannon, Acta Crystallogr., Sect. A: Cryst. Phys., Diffr., Theor., Gen. Crystallogr A29 (1973) 266–282.
[23] Z.L. Gong, Y. Yang, Energy Environ. Sci. 4 (2011) 3223–3242.